Photodiagnosis and Photodynamic Therapy 27 (2019) 27–33

Contents lists available at ScienceDirect

Photodiagnosis and Photodynamic Therapy

journal homepage: www.elsevier.com/locate/pdpdt

Sonodynamic cancer therapy by a nickel ferrite/carbon nanocomposite on melanoma tumor: In vitro and in vivo studies

M. Gorgizadeh[a,b], N. Azarpira[b,c], M. Lotfi[b,d], F. Daneshvar[a,b], F. Salehi[a,b], N. Sattarahmady[a,b,*]

[a] Department of Medical Physics, School of Medicine, Shiraz University of Medical Sciences, Shiraz, Iran
[b] Nanomedicine and Nanobiology Research Center, Shiraz University of Medical Sciences, Shiraz, Iran
[c] Transplant Research Center, Shiraz University of Medical Sciences, Shiraz, Iran
[d] Department of Radiology, Shiraz University of Medical Sciences, Shiraz, Iran

ARTICLE INFO

Keywords:
Ultrasound therapy
Melanoma cancer
Ni-ferrite
Carbon nanocomposite
Contrast agent

ABSTRACT

Reactive oxygen species (ROS)-mediated cancer therapy using light or ultrasound (US) has been widely approached as a non-invasive and inspiring alternative treatment. Sonodynamic therapy (SDT), a non-invasive therapeutic modality of cancer, is an outcome of low-intensity US effect on cancer cells using a sonosensitizer, which results in heat and ROS production followed by cell death. The aim of this study was synthesis, characterization and cancer SDT application of a nickel ferrite/carbon nanocomposite ($NiFe_2O_4$/C), as a sonosensitizer. SDT was carried out by applying a 1.0-MHz US radiation at 1.0 W cm^{-2} of power density and 100% pulse ratio for 60 s. A significant C540 (B16/F10) cell killing was observed in vitro due to ROS production of 100 µg mL^{-1} of $NiFe_2O_4$/C upon SDT. In addition, SDT of melanoma cancer in a mouse model using intratumorally injected $NiFe_2O_4$/C of 100 µg mL^{-1} produced remarkable efficacious recovery in the tumor and significant necrosis (up to 60%) in histological assessments, while injection of $NiFe_2O_4$/C or US irradiation alone induced no healing effect. Therefore, SDT using $NiFe_2O_4$/C attained success in destroying melanoma cancer and can be developed and introduced as an alternative treatment strategy for melanoma cancer. In furtherance of SDT, magnetic resonance (MR) imaging (1.5 T) in an agarose phantom indicated the effectiveness of $NiFe_2O_4$/C as a negative contrast agent in transverse relaxation time-weighted imaging with a corresponding relaxation rate (r_2) of 78.9 mmol L^{-1} s^{-1}. The results confirmed the applicability of the nanocomposite as a theranostics agent for simultaneous SDT and MR imaging.

1. Introduction

Cancer is often a grim threatening disease.. Conventional procedures for cancer treatment include surgery, radiotherapy, and chemotherapy which are often inadequate and with side effects [1–3]. Finding alternative and efficient tumor treatment methods using various sources of energy is, therefore, a significant plan in tumor treatment. Applying radio-frequency, microwave, ultrasound (US) and laser for tumor eradication is in progress in the medical and scientific community 4]. These treatments can induce cell annihilation with membrane and macromolecules destruction via thermal or non-thermal mechanisms [5].

Recently, sonodynamic therapy (SDT) has been introduced as a non-invasive tumor treatment and acts through the activation effect of ultrasound waves on chemical compounds (sonosensitizers) via acoustic cavitation in the tumor cells [6,7]. US, depending on its intensity and frequency, generates heat and also has mechanical impacts on tissues [6,7]. Intensities around 2.0 W cm^{-2} have been considered as the boundary of low and high levels of US accompanied with functional changes and structural alterations in the tissues, respectively [7].

US waves, depending to frequencies, intensities and exposure time, affect the tissues in thermal or non-thermal modes. In the thermal mode, a high-intensity pulsed or continuous US wave induces thermal effects in the tissues [8]. On the other hand, non-thermal interaction of US waves with liquid bulks in the tissues leads to formation of gas- or vapor-filled cavities (bubbles) which are known as acoustic cavitation. Acoustic cavitation leads to interaction and permeability changes in the cell membrane. During the cavitation process, bubble nucleation is followed by growth and then collapse, depending on the environment. Based on the stability of these bubbles, non-inertial or inertial cavitations are defined. In non-inertial cavitation, the bubbles preserve and oscillate in an equilibrium radius that transports the mechanical stress

* Corresponding author.
E-mail addresses: nsattar@sums.ac.ir, sattarahmady@yahoo.com (N. Sattarahmady).

https://doi.org/10.1016/j.pdpdt.2019.05.023
Received 11 January 2019; Received in revised form 26 March 2019; Accepted 17 May 2019
Available online 19 May 2019

to the medium. However in inertial cavitation, the bubbles expand to a maximum size, and then rapidly collapse [9–11]. In this route, diffused energy of US is converted into augmentation of heat and pressure in the imploding bubble (cavities) that induce physical events in the surrounding area [12]. In this way, sonochemical reactions such as light emission occurred both within and surface of the bubbles [11].

In SDT, the sonosensitizers should have a minimal cytotoxicity effects, and kill the cells upon US stimulation. Protoporphyrin IX and some other light sensitizaing agents can act as sonnosensitizers in SDT; they interact with the molecular oxygen and generate reactive oxygen species (ROS) to kill the cells [13]. One of the drawbacks of the sonosensitizers is their hydrophobic trait that limits their bioavailability [13]. Nevertheless, nanoformulations of these sensitizers can improve their efficacy by increment in their water solubility [14]. These nanoformulations can deliver sonosensitizers and enhance the efficacy of low-intensity SDT through increase in the possibility of bubbles formation [15]. Along this line, various nanomaterials have been employed as proper sonosensitizers, such as gold [16] and TiO_2 nanoparticles [17]. Advances in novel nanostructured sonosensitizers with the ability of ROS and heat production upon exposure to US can improve the efficacy of SDT. There have been efforts to introduce innovative nanomaterials as sonosensitizers in SDT [16,17].

Today, magnetic nanomaterials have been prepared in combination with other nanomaterials in complex structures for applications in diagnostics, therapy and theranostics [18–21]. These nanomaterials have been applied as contrast agents in magnetic resonance (MR) imaging, magnetic separations in biotechnological purposes, cell tracking, magnetic drug delivery, and hyperthermia [19–22]. For the imaging purposes, contrast agents intensify the signal-to-noise ratio in MR imaging to discriminate the two adjoining tissues. Decreasing relaxation times of longitudinal (T_1) and transverse (T_2) of the water protons by positive contrast or negative contrast agents redounds to increase in the images' contrast.

Ferrite nanoparticles as a kind of magnetic nanoparticles with the formula of AFe_2O_4 (A: Co, Ni, Zn, etc.) have different applications in medical sciences [18,19,21,23]. Ferrite nanoparticles have been applied as T_2 contrast enhancement agents [21]. On the other side, researchers have had a special look at carbon nanomaterials and their uses in medicine [18,24,25]. Carbon nanomaterials are remarkable in terms of thermal and electrical conductivities, mechanical stiffness, photostability and heat photoconversion [25–29]. Also, carbon-based nanomaterials were applied for sonodynamically cancer killing [30,31], and application of carbonaceous materials in SDT was very limited in the literature. Integration of metal oxide nanostructures with carboanceous nanomaterials produced composite structures with exploited properties of both components with theranostic applications [32].

In this study, a nickel ferrite/carbon nanocomposite ($NiFe_2O_4$/C) was synthesized, characterized and applied as a sonosensitizer for killing the melanoma cell line and a tumor destruction model in balb/c mice. Cell viability, ROS production and histophatological outcomes were presented.

2. Materials and methods

2.1. Materials

All chemicals were purchased from Sigma Chemicals Co. (USA), Scharlau Chemie Co. (Spain) or Merck Co. (Germany) and used without further purification. Deionized water (DIW) was used throughout the study.

2.2. Synthesis and characterization of $NiFe_2O_4$/C

A mix solution of $NiCl_2.6H_2O$ (0.4 mmol L^{-1}), $FeSO_4.7H_2O$ (0.8 mmol L^{-1}) and dopamine (0.8 mg mL^{-1} in a 5:1 water:ethanol mixture) was reached to pH = 8.5 with Tris buffer and stirred for three days at room temperature. Then, the solution was centrifuged and washed five times with DIW. After drying, the sample was calcined at 600 °C at a heating rate of 2 °C min^{-1} for 2 h under an Ar atmosphere.

The size and morphology of $NiFe_2O_4$/C were evaluated by transmission electron microscopy (TEM, Zeiss, EM10C, Germany) with an accelerating voltage of 80 kV. For TEM sample preparation, a carbon formvar-coated copper grid was employed and a diluted dispersion of $NiFe_2O_4$/C in water was loaded. Elemental CHNSO analysis was performed for determination of the carbon content of $NiFe_2O_4$/C, using a Costech ECS 4010 CHNSO analyzer (Italy). Magnetic properties of $NiFe_2O_4$/C were studied by a vibrating sample magnetometer (VSM) of Meghnatis Daghigh Kavir Co. instrument (Iran) at room temperature. The external magnetic field varied from -20 to 20 kOe.

2.3. Cell line and animal preparations

Mouse malignant melanoma cell line C540 (B16/F10) was prepared from National Cell bank of Iran (NCBI) of Pasteur Institute of Iran (http://ncbi.pasteur.ac.ir/). The cells were grown in Roswell Park Memorial Institute-1640 (RPMI) medium supplemented with 10% fetal bovine serum (FBS) and 1% antibiotic (penicillin-streptomycin) in a humidified cell culture incubator at 37 °C, 5% CO_2.

Eight male balb/c inbred mice (4-week old, body weight of ˜20 g) were prepared from the center of comparative and experimental medicine, Shiraz University of Medical Sciences. The procedure was followed in accordance with the rules of the committee on the Ethics of Animal Experiments of Shiraz University of Medical Sciences. Maintenance cages of animals were fixed at a controlled temperature (24 ± 2 °C) and humidity (40-70%) with weekly floor exchange. They had free access to water and standard pelleted laboratory animal diets. A 12:12 light:dark cycle was followed in the mentioned animal vivarium.

2.4. C540 (B16/F10) cell viability

Cell viability was specified upon cell treatment with $NiFe_2O_4$/C, US exposure and SDT (both treatment with $NiFe_2O_4$/C and US exposure). C540 (B16/F10) cells were seeded into 24-well culture plates for 24 h to adhere the cells in a population of 1.0×10^4 cells $well^{-1}$. These cells were then divided into different groups as follows: U-N_{cell} (untreated group or control cells), U^+N_{cell} (US exposure cells), U-N^+_{cell} ($NiFe_2O_4$/C treated cells), and $U^+N^+_{cell}$ (sonodynamic treated cells). In the U-N^+_{cell} and $U^+N^+_{cell}$ groups, $NiFe_2O_4$/C of different concentrations (10, 25, 50, and 100 μg mL^{-1}) was added into the cell medium. In the U-N_{cell} and U^+N_{cell} groups, DIW with equivalent volumes of $NiFe_2O_4$/C was used. Following 4 h incubation [19,33–36] (with $NiFe_2O_4$/C or DIW), the cells were exposed to US for 60 s in the U^+N_{cell} and $U^+N^+_{cell}$ groups. To attain it, an ultrasonic apparatus (Novin, Iran) was used wherein the US transducer placed under the 24-well culture plates. The surface of transducer was covered with a gel. US was then irradiated from the bottom of the dishes with the following conditions: frequency of 1.0 MHz, output power of 1.0 W cm^{-2}, and different pulse ratios of 10, 50 and 100% [33,37–39]. Incubation of the group cells was then continued overnight at 37 °C, 5% CO_2. It was followed by cell viability measurement by the 3-(4,5-dimethylthiazol-2-yl)-2,5-diphenyltetrazolium bromide (MTT) assay. For the assay, the cells medium was substituted by MTT (100 μL of 0.5 mg mL^{-1} dissolved in PBS) and incubated for 4 h at 37 °C in dark. Then, the medium was centrifuged at 1800 rpm for 10 min, and the supernatant was discarded following the addition of 100 μL dimethyl sulfoxide (DMSO) to dissolve the MTT formazan crystals. The mixture was centrifuged again at 3500 rpm for 3 min and the absorbance values of the supernatants were measured at 570 nm, using the microplate reader (Biotek, USA). Cell viability was expressed as the ratio of the 570-nm absorbance of the treated to control cells. Measurement for each group was run in triplicate.

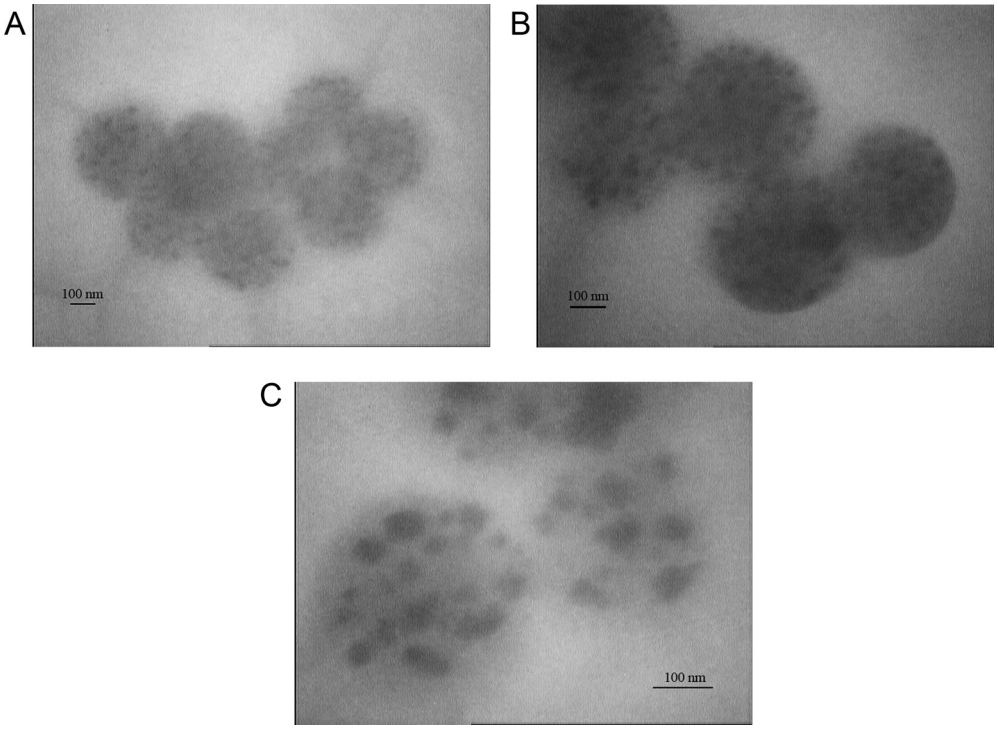

Fig. 1. TEM image of $NiFe_2O_4$/C.

2.5. Detection of intracellular ROS production in C540 (B16/F10) cells

Fluorescence intensity (FI) of dichlorofluorescein (DCF) was measured as an indicator of intracellular ROS production. In this assay, 2,7-DCF diacetate (DCFH-DA) enters the cells, and upon oxidation by intracellular ROS, it is cleaved, de-esterified with endogenous esterases and converted into the fluorescent compound DCF. Different groups of C540 (B16/F10) cells including $U^-N^-_{cell}$, $U^+N^-_{cell}$ (at a 100% pulse ratio), $U^-N^+_{cell}$ (treated with 100 μg mL^{-1} $NiFe_2O_4$/C), and $U^+N^+_{cell}$ (at a 100% pulse ratio and 100 μg mL^{-1} $NiFe_2O_4$/C) were incubated with $NiFe_2O_4$/C or DIW, and after 3.5 h incubation, 100 μL of a fresh DCHF-DA solution (50 μmol L^{-1}) was added to each well. After 30 min, the cells were or were not treated with US. After that, the cells were washed three times with PBS to remove the extracellular DCF. Then, 100 μL of a lysis buffer (containing 150 mmol L^{-1} NaCl, 0.1% Triton X-100, 50 mmol L^{-1} Tris-HCl, pH 8.0) was added to each well, and after 30 min, the intensity of fluorescence emission at 520 nm was measured upon excitation at 485 nm within 96-well black plates, using the microplate reader (Biotek, USA).

2.6. Statistical analysis

At least three parallel measurements were done for each quantity. Non-parametric Kruskal-Wallis test and *t*-test were used to analyze the statistical significance of the results using GraphPad (Prism 6) software. A p-value of less than 0.05 was considered statistically significant.

2.7. Tumor implantation and SDT of melanoma tumor in mice

Melanoma cancer cells (1.3×10^6) in 100 μL PBS were subcutaneously injected into subaxillary of anesthetized male balb/c inbred mice, and a tumor volume of 100 mm^3 was attained after 2 weeks. Then, melanoma-bearing animal models were divided into different groups as follows: $U^-N^-_{mouse}$ (untreated group or control mice, injection of 200 μL saline), $U^+N\text{-}_{mouse}$ (US exposure tumors), $U^-N^+_{mouse}$ (intratumorally $NiFe_2O_4$/C injected mice), and U^+N^+ $_{mouse}$ (sonodynamic treated mice). In the $U^+N\text{-}_{mouse}$ and $U^+N^+_{mouse}$ groups, the mice were exposed to US for 60 s at a frequency of 1.0 MHz, output power of 1.0 W cm^{-2}, and pulse ratio of 100%. In the U-N^+_{mouse} and $U^+N^+_{mouse}$ groups, a suspension of $NiFe_2O_4$/C in PBS (1.0 mg mL^{-1}, 200 μL, ~10 mg kg^{-1} $mouse^{-1}$) was locally injected in the tumors of the animals. It should be noted that intratumoral injection was performed two times into two different locations of the tumor (100 μL each) with the final volume of injection of 200 μL.

Animal treatment was performed followed by anesthesia with a mixture of ketamin (10%) and xylazine (2%). After 24 h, the mice were sacrificed and their tumor was excised for H&E staining.

2.8. Histological analyses of tumor tissues

The removed tissues were fixed with a 10% formalin buffered solution and embedded routinely into paraffin. Paraffin sections of 3–5 μm thickness on glass slides were stained with hematoxylin and eosin (H&E) and analyzed by a digital microscope (Olympus, Japan). In the slides of the tumor tissues, the necrotic surface area was estimated by measuring graticule for each animal group. The percentage of necrosis against the whole tumor area was estimated and graded as grade 1 (< 10%), grade 2 (11–20%), grade 3 (21–40%), or grade 4 (41–70%) necrosis.

2.9. MR imaging studies using a phantom

As a T_2-weighted MR imaging contrast agent, $NiFe_2O_4$/C was evaluated using a 1.5 T MagnetomAvanto, Siemens (Germany) MR instrument equipped with a knee coil with Turbo Spin-Echo and FLASH pulse sequence. Suspensions of different concentrations of $NiFe_2O_4$/C were prepared in agarose gel (1% w/v) in a 96-well plate. For T_2 of proton determination, the time of echo (TE) varied from 22 to 176 ms, and time of repetition (TR) was selected equal to 1800 ms. Scan parameters were set as follows: field of view (FOV) was 160 × 160 mm^2 and slice thickness was 3 mm. The value of relaxivity (r_2) was calculated by curve fitting of the plots of $1/T_2$ versus the concentration of iron and nickel species in the $NiFe_2O_4$/C.

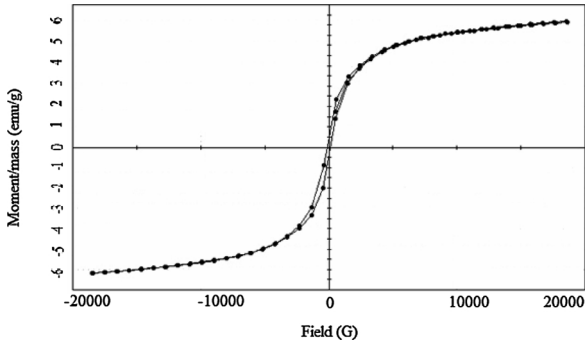

Fig. 2. Magnetization curve of $NiFe_2O_4$/C.

3. Results

3.1. Characterization of $NiFe_2O_4$/C

Fig. 1 shows TEM images of $NiFe_2O_4$/C recorded at different magnifications. The TEM images of $NiFe_2O_4$/C revealed that the sample had a spherical shape with a uniform and regular morphology. $NiFe_2O_4$/C comprised spherical carbon with low-contrast signatures in the images due to the low-molecular weight of its entity accompanied by uniformly embedded high-contrast features arising from nanoparticles of $NiFe_2O_4$ as the consequence of higher molecular weight of nickel and iron. While the whole structure of $NiFe_2O_4$/C had an average diameter of 381.6 ± 33.3 nm, the magnetic nanoparticles represented an average diameter of 38.2 ± 7.3 nm.

Elemental analysis of $NiFe_2O_4$/C indicated that the percentages of the C, H and N elements in $NiFe_2O_4$/C were 62.2, 1.8 and 6.3%, respectively. Therefore, the $NiFe_2O_4$/C contained 62% carbon and 38% $NiFe_2O_4$, respectively. Fig. 2 depicts magnetization behavior of $NiFe_2O_4$/C. Superparamagnetic behavior of the $NiFe_2O_4$/C can be deduced from the pattern of the hysteresis loop. The magnetic parameters for $NiFe_2O_4$/C were obtained from hysteresis data and reported in Table 1.

3.2. Cytotoxicity, US and SDT efficacies and ROS production evaluations in vitro

In vitro cytotoxicity and US and SDT effects of different concentrations of $NiFe_2O_4$/C were examined by the MTT assay. Samples in the groups of $U^-N^+_{cell}$ and $U^+N^+_{cell}$ were treated by $NiFe_2O_4$/C of 10, 25, 50, and 100 μg mL^{-1}. Samples in the groups of $U^+N^-_{cell}$ and $U^+N^+_{cell}$ were irradiated by US at 1.0 MHz and 1.0 W cm^{-2}, in different pulse ratios of 10%, 50% and 100% for 60 s. Fig. 3 represents the viability percentage of the cells (relative to untreated cells) treated with $NiFe_2O_4$/C at three different pulse ratios of US exposure of 10% (A), 50% (B), and 100% (C). We observed a concentration-dependent toxicity for the cells, and there was up to 58% viability in the presence of 100 μg mL^{-1} $NiFe_2O_4$/C

Table 1
Magnetic parameters of $NiFe_2O_4$/C obtained from hysteresis data.

M_s /emu g^{-1}	H_c / G	M_r / emu g^{-1}	R	n_B
6.17	131	0.46	74.4 × 10^{-3}	0.26

Abbreviations:
M_s: Saturation magnetization.
H_c: Coercivity.
M_r: Remanence magnetization.
R: Remanent ratio, M_r/M_s.
n_B: Magnetic moment per formula unit in Bohr magneton calculated from saturation magnetization of the hysteresis loop using the equation [33]: $n_B = (M_w M_s)/5585$where M_w is the molecular weight and the coefficient of 5585 is the magnetic factor.

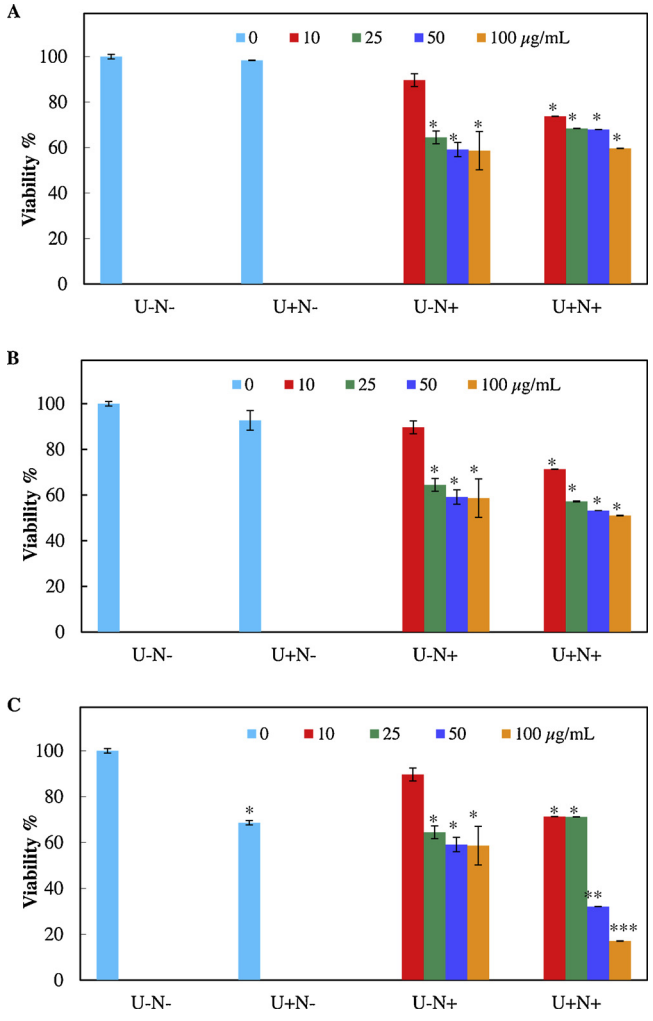

Fig. 3. Percentage of C540 (B16/F10) cell viability in $U^-N^-_{cell}$ (untreated groups, control), $U^+N^-_{cell}$ (treated with US exposure), U^-N+_{cell} (treated with $NiFe_2O_4$/C), $U^+N^+_{cell}$ (US exposure after treated with $NiFe_2O_4$/C). Concentrations of $NiFe_2O_4$/C were considered 10, 25, 50, and 100 μg mL^{-1}, and the condition of US radiation was frequency, 1.0 MHz; output power: 1.0 W cm^{-2}, in different pulse ratios of A) 10%, B) 50% and C) 100%.* Indicates significant differences ($p < 0.05$). ** Indicates very significant differences ($p < 0.01$). *** Indicates the most significant differences ($p < 0.001$).

(Fig. 3). There was a dose dependent toxicity for $NiFe_2O_4$/C, and it was enhanced upon US exposure. The difference in the viability between the groups $U^-N^+_{cell}$ and $U^+N^+_{cell}$ at 10% and 50% pulse ratio was not significant (Kruskal-Wallis test, p-value > 0.05). The results also showed a decrease in the cell viability upon increasing pulse ratio of US irradiation in $U^+N^-_{cell}$. The results indicated that in the $U^+N^+_{cell}$ and at 100% pulse ratio the relative values of cell viabilities for the $NiFe_2O_4$/C concentrations of 50 and 100 μg mL^{-1} were 32 and 17%, respectively. In addition, statistical analyses confirmed that there were significant differences between the two cell viability values together; also, these values were compared to cell viabilities of the other groups ($U^-N^-_{cell}$, $U^+N^-_{cell}$, and $U^-N^+_{cell}$), based on Kruskal-Wallis test (p-value < 0.05).

Intracellular ROS formation during treatment was evaluated using fluorescence intensity of DCF. DCFH-DA passively penetrates into the cells and is deacetylated by esterases to non-fluorescent DCFH. Intracellular ROS interacts with DCFH and produces fluorescent DCF with emission at 520 nm. Control cells had low fluorescence intensities at 520 nm that was considered as background. Fig. 4 shows the intensity of fluorescence emission at 520 nm for $U^+N^-_{cell}$, $U^-N^+_{cell}$, and $U^+N^+_{cell}$. As shown in this Figure, after treatment of the cells,

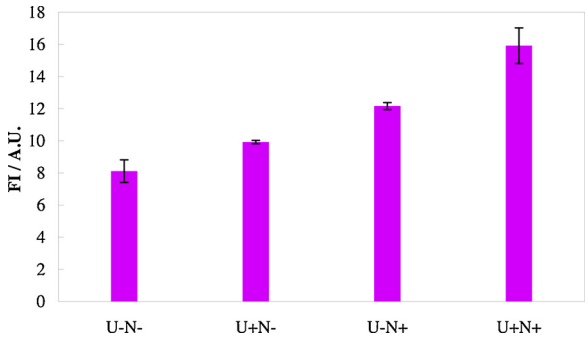

Fig. 4. FI of DCF of C540 (B16/F10) cell in the $U^{-}N^{-}_{cell}$, $U^{+}N^{-}_{cell}$, $U^{-}N^{+}_{cell}$, and $U^{+}N^{+}_{cell}$ groups.

fluorescence intensities and intracellular ROS levels in $U^{+}N^{+}_{cell}$ increased significantly, compared to $U^{-}N^{-}_{cell}$, while the fluorescence intensity of $U^{-}N^{+}_{cell}$ and $U^{+}N^{-}_{cell}$ was a little greater than $U^{-}N^{-}_{cell}$. Therefore, more ROS formation occurred in the SDT group cells that induced oxidation of intracellular DNA and proteins [40] with a higher killing rate in cancer cells.

3.3. SDT efficacy evaluations in vivo

SDT study was managed in vivo on melanoma bearing mice model. Animals were divided into groups of $U^{-}N^{-}_{mouse}$, $U^{+}N^{-}_{mouse}$, $U^{-}N^{+}_{mouse}$, and $U^{+}N^{+}_{mouse}$. When melanoma tumors grew up to about 100 mm^3 in volume, treatment was started. 200 μL of 1.0 mg mL^{-1} of $NiFe_2O_4$/C suspensions was intratumorally injected into the mice in the $U^{-}N^{+}_{mouse}$, and $U^{+}N^{+}_{mouse}$. Subsequently, the tumor of groups $U^{+}N^{-}_{mouse}$ and $U^{+}N^{+}_{mouse}$ was exposed to US (at 1.0 MHz, 1.0 W cm^{-2}, 100% duty for 60 s). No death and destructive influence was noticed after $NiFe_2O_4$/C suspensions injection, with or without US exposure in the treated animals. Fig. 5 shows the slides of H&E-stained tumor of animals in groups of $U^{-}N^{-}_{mouse}$ (A), $U^{+}N^{-}_{mouse}$ (B), $U^{-}N^{+}_{mouse}$ (C), and $U^{+}N^{+}_{mouse}$ (D) that were prepared 24 h after treatment. In agreement with H&E-staining slides in Fig. 5A, B and C, viable malignant melanoma cells with brown pigment and less than 10% necrosis were observed in the tumor of the animals in $U^{-}N^{-}_{mouse}$, $U^{+}N^{-}_{mouse}$ and $U^{-}N^{+}_{mouse}$ groups (grade one necrosis). These results indicated low toxic effect of US exposure and $NiFe_2O_4$/C affection alone. Fig. 5D shows H&E-stained slides of the tumor of $U^{+}N^{+}_{mouse}$ group, indicating that SDT induces ~ 60% necrosis in the tumor of the animals (grade four necrosis > 50%).

3.4. MR imaging using a phantom

$NiFe_2O_4$/C was applied as a contrast agent in MR imaging in an agar phantom, using a 1.5-T MR instrument. Fig. 6A shows T_2 (spin-echo pulse sequence, TR = 1800 ms, TE = 88 ms) weighted images of $NiFe_2O_4$/C. The results indicated that the signal intensity in T_2 images decreased upon increase in the $NiFe_2O_4$/C concentration because of T_2 shortening. Also, Fig. 6B shows dependency of relaxation rate on the Fe + Ni concentration in $NiFe_2O_4$/C resulting in a relaxation rate (r_2) value of 78.9 mmol L^{-1} s^{-1}.

4. Discussion

SDT is a promising treatment approach by using low-intensity ultrasound and a sonosensitizer, which generates heat and ROS. US can penetrate deep into the tissues, relative to light in phototherapy approaches, without energy wastage. Hence, in US-based therapies, the problem of limited penetration of near-infrared light in photodynamic therapy is resolved. SDT has also advantages of safely passing from several layers of tissues and definitely focuses with high spatial precision on the sonosensitizer within the tumors [41,42]. However, applying US in cancer treatment is on increase in clinics [42], and

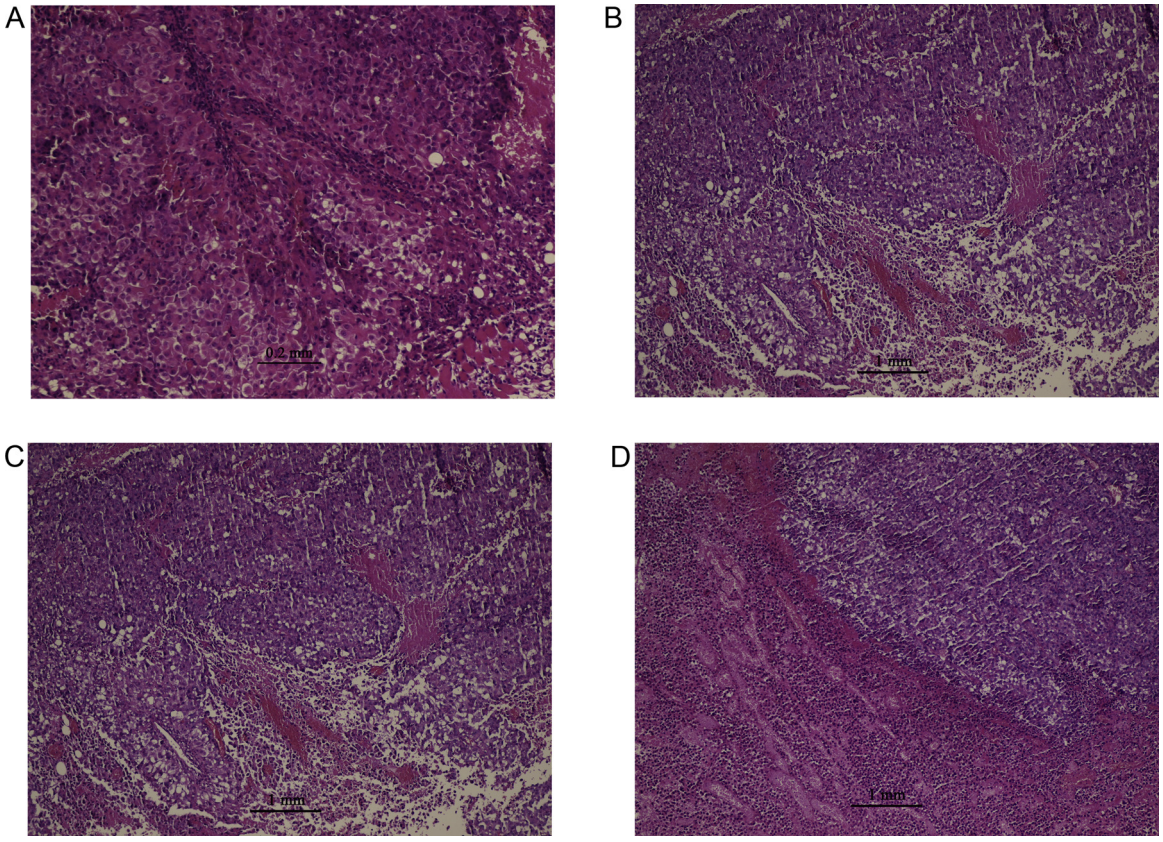

Fig. 5. H&E stained slide of tumors in (A) $U^{-}N^{-}_{mouse}$, (B) $U^{+}N^{-}_{mouse}$, (C) $U^{-}N^{+}_{mouse}$, and (D) $U^{+}N^{+}_{mouse}$.

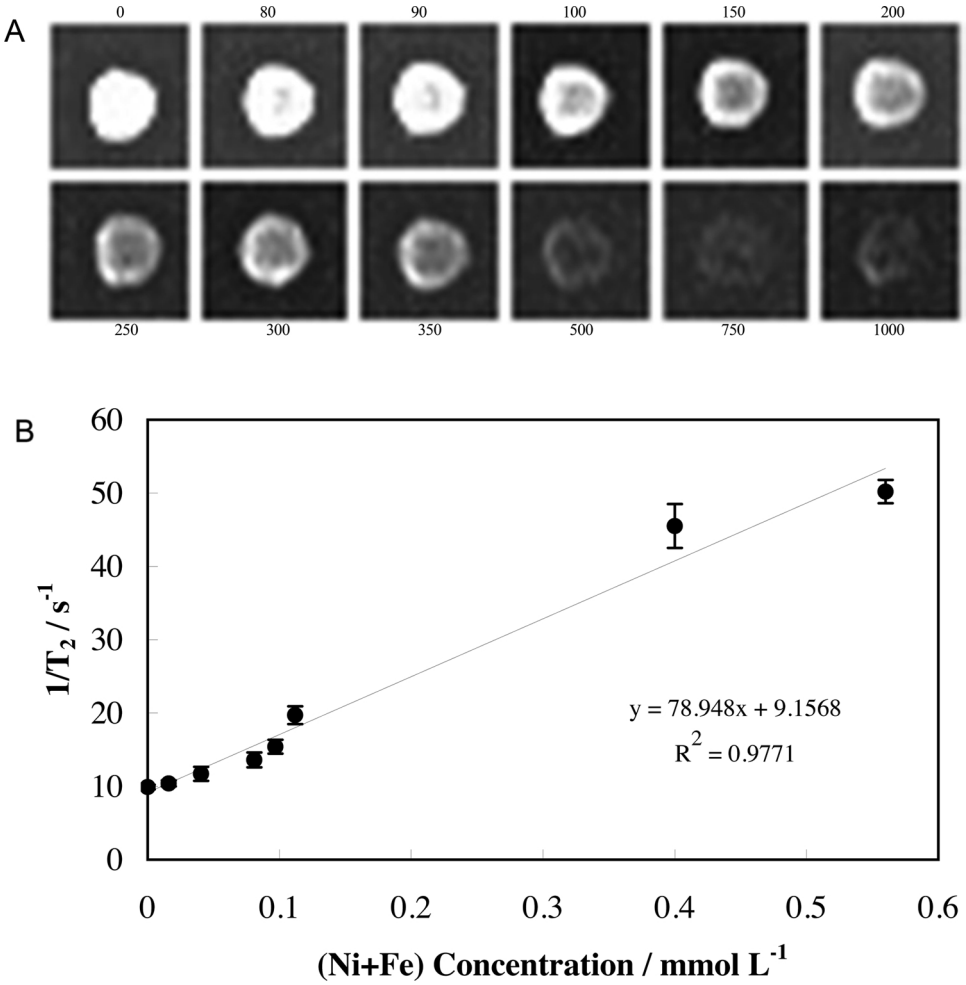

Fig. 6. (A) Signal intensity of T_2-weighted images at different Fe + Ni contents of $NiFe_2O_4$/C (0–1000 μg mL^{-1}). (B) Dependency of the relaxation rate on the Fe + Ni content of $NiFe_2O_4$/C. From up left to right: 0, 80, 90, 100, 150 and 200 μg mL^{-1}. From down left to right: 250, 300, 350, 500, 750 and 1000 μg mL^{-1}.

sonosensitizers with higher quantum yield can improve its efficacy. On the other hand, high cavitation threshold and small therapeutic region are the major problems in SDT. For subtracting the cavitation threshold of the ultrasound waves, nanomaterials of TiO_2, silica and iron oxide have been effective as cavitation promoters, and have enhanced the singlet oxygen production [43–45]. Stimulation of TiO_2-based nanomaterials as sonosensitizers with US promoted cavitation, bubble and OH radicals generation [46,47]. Pt, Au and Ag can also improve the efficacy of TiO_2 nanoparticles as sonosensitizers [48–51]. Chen et al. synthesized mesoporous silica on reduced grapheme oxide nanosheets capped with Rose Bengal-polyethylene glycol-conjugated iron oxide nanoparticles that were guided with magnetic force in the tumor area, and produced heat and ROS under a focused US irradiation [44].

The obtained SDT results showed increment in the fluorescence intensity of DCF in $U^+N^+_{cell}$, compared to $U^-N^-_{cell}$. On the other hand, the results indicated that ROS generation in $U^+N^-_{cell}$ and $U^-N^+_{cell}$ (the cells exposed to $NiFe_2O_4$/C or US alone) was higher than $U^-N^-_{cell}$, indicating that $NiFe_2O_4$/C and US exposure alone could promote ROS production in the cells. Owing to the fact that US exposure at conditions employed in this study (frequency of 1.0 MHz and output power of 1.0 W cm^{-2}) produces inertial cavitation in a cell culture or tumor [52], it would be expected that cavitation effect was dominated in SDT. US energy was converted to heat, and more ROS was produced in the $U^+N^+_{cell}$. Measurement of the cell viability by the MTT assay pointed out higher cytotoxicity of $NiFe_2O_4$/C upon US irradiation. Cytotoxic effect was due to the thermal effect and ROS generation. In vivo study showed that in spite of non-toxic effect of the injected dose of $NiFe_2O_4$/C in animals, 60% necrosis occurred the in tumor area of the $U^+N^+_{mouse}$. After the first day post-treatment, histopathology results indicated that SDT of $NiFe_2O_4$/C could be applied as an invasive and inspiring alternative for melanoma cancer treatment. $NiFe_2O_4$/C is composed of a ferrite as superparamagnic nanoparticles [21] with a diameter of 38.2 ± 7.3 nm, and carbon microspheres as an effective photo- and US-absorber agent [24,30,31] with a diameter of 381.6 ± 33.3 nm. Ferrites can act as both hyperthermia and contrast agents in MR imaging. Combination of these materials in $NiFe_2O_4$/C provided an agent with the functions of magnetic hyperthermia, MR contrast imaging and SDT properties for potential theranostic applications. Also, the results indicated that $NiFe_2O_4$/C could be applied as contrast agent in MR imaging with a concentration-dependent reduction in the signal intensity of T_2-weighted images. The r_2 value for $NiFe_2O_4$/C indicated that the nanocomposite is an excellent negative contrast in MR imaging.

5. Conclusion

$NiFe_2O_4$/C was introduced as a new sonosensitizer for SDT of melanoma cancer in the cell line and mouse models. Based on the results, radiation of US into $NiFe_2O_4$/C effectively induced cavitation formation and ROS production. Cell toxicity results showed that $NiFe_2O_4$/C represented dose-dependent toxicity toward C540 (B16/F10) cells upon exposure to US. SDT effect of $NiFe_2O_4$/C was remarkably important on the melanoma treatment of the tumor in the mice model, compared to animals experiencing just US or $NiFe_2O_4$/C injection. The nanocomposite has the advantage of applicability for both diagnostics and

therapy.

Ethical statement

This study was approved by the Committee on the Ethics of Animal Experiments of Shiraz University of Medical Sciences.

Conflict of interest

The authors have no conflict of interest.

Acknowledgments

We would also like to thank the Research Council of Shiraz University of Medical Sciences (14340) for supporting this research.

References

[1] L. Wyld, R.A. Audisio, G.J. Poston, The evolution of cancer surgery and future perspectives, Nat. Rev. Clin. Oncol. 12 (2015) 115–124.
[2] M.S. Moran, Radiation therapy in the locoregional treatment of triple-negative breast cancer, Lancet Oncol. 16 (2015) 113–122.
[3] G.L. Deng, S. Zeng, H. Shen, Chemotherapy and target therapy for hepatocellular carcinoma: new advances and challenges, World J. Hepatol. 7 (2015) 787–798.
[4] A. Sahu, W.I. Choi, J.H. Lee, G. Tae, Graphene oxide mediated delivery of methylene blue for combined photodynamic and photothermal therapy, Biomaterials 34 (2013) 6239–6248.
[5] S.J. Mousavy, G.H. Riazi, M. Kamarei, H. Aliakbarian, N. Sattarahmady, A. Sharifizadeh, S. Safarian, F. Ahmad, A.A. Moosavi-Movahedi, Effects of mobile phone radiofrequency on the structure and function of the normal human hemoglobin, Int. J. Biol. Macromol. 44 (2009) 278–285.
[6] K. Tachibana, L. Feril Jr, Y. Ikeda-Dantsuji, Sonodynamic therapy, Ultrasonics 48 (2008) 253–259.
[7] T. Yu, Z. Wang, T.J. Mason, A review of research into the uses of low level ultrasound in cancer therapy, Ultrason. Sonochem. 11 (2004) 95–103.
[8] K. Tachibana, L. Feril Jr, Y. Ikeda-Dantsuji, Sonodynamic therapy, Ultrasonics 48 (2008) 253–259.
[9] L. Serpe, F. Foglietta, R. Canaparo, Nanosonotechnology: the next challenge in cancer sonodynamic therapy, Nanotechnol. Rev. 1 (2012) 173–182.
[10] K.S. Suslick, Sonochemistry, Science 247 (1990) 1439–1445.
[11] K.S. Suslick, S.J. Doktycz, E.B. Flint, On the origin of sonoluminescence and sonochemistry, Ultrasonics 28 (1990) 280–290.
[12] K.S. Suslick, D.J. Flannigan, Inside a collapsing bubble: sonoluminescence and the conditions during cavitation, Annu. Rev. Phys. Chem. 59 (2008) 659–683.
[13] Y. Meng, C. Zou, R. Madiyalakan, T. Woo, M. Huang, X. Yang, E. Swanson, J. Che, J.Z. Xing, Water-soluble and biocompatible sono/photosensitizer nanoparticles for enhanced cancer therapy, Nanomedicine 5 (2010) 1559–1569.
[14] S.J. Yang, M.J. Shieh, F.H. Lin, P.J. Lou, C.L. Peng, M.F. Wei, C.J. Yao, P.S. Lai, T.H. Young, Colorectal cancer cell detection by 5-aminolaevulinic acid-loaded chitosan nanoparticles, Cancer Lett. 273 (2009) 210–220.
[15] T. Tuziuti, K. Yasui, M. Sivakumar, Y. Iida, N. Miyoshi, Correlation between cavitation noise and yield enhancement of sonochemical reaction by particle addition, J. Phys. Chem. A 109 (2005) 4869–4872.
[16] C. Brazzale, R. Canaparo, L. Racca, F. Foglietta, G. Durando, R. Fantozzi, P. Caliceti, S. Salmaso, L. Serpe, Enhanced selective sonosensitizing efficacy of ultrasound-based anticancer treatment by targeted gold nanoparticles, Nanomedicine 11 (2016) 3053–3070.
[17] K. Ninomiya, K. Noda, C. Ogino, S. Kuroda, N. Shimizu, Enhanced OH radical generation by dual-frequency ultrasound with TiO2 nanoparticles: its application to targeted sonodynamic therapy, Ultrason. Sonochem. 21 (2014) 289–294.
[18] M. Negahdary, H. Heli, Applications of nanoflowers in biomedicine, Recent Pat. Nanotechnol. 12 (2018) 22–33.
[19] M. Gorgizadeh, N. Azarpira, N. Sattarahmady, In vitro and in vivo tumor annihilation by near-infrared photothermal effect of a NiFe2O4/C nanocomposite, Colloids Surf. B 170 (2018) 393–400.
[20] N. Sattarahmady, N. Azarpira, A. Hosseinpour, H. Heli, T. Zare, Albumin coated arginine-capped magnetite nanoparticles as a paclitaxel vehicle: physicochemical characterizations and in vitro evaluation, J. Drug Deliv. Sci. Technol. 36 (2016) 68–74.
[21] N. Sattarahmady, M. Heidari, T. Zare, M. Lotfi, H. Heli, Zinc-nickel ferrite nanoparticles as a contrast agent in magnetic resonance imaging, Appl. Magn. Reson. 47 (2016) 925–935.
[22] J.E. Rosen, L. Chan, D.B. Shieh, F.X. Gu, Iron oxide nanoparticles for targeted cancer imaging and diagnostics, Nanomed. Nanotechnol. Biol. Med. 8 (2012) 275–290.
[23] M.A. Willard, L.K. Kurihara, E.E. Carpenter, S. Calvin, V.G. Harris, Chemically prepared magnetic nanoparticles, Int. Mater. Rev. 49 (2004) 125–170.
[24] N. Sattarahmady, M. Rezaie-Yazdi, G.H. Tondro, N. Akbari, Bactericidal laser ablation of carbon dots: an in vitro study on wild-type and antibiotic-resistant Staphylococcus aureus, J. Photochem. Photobiol. B 166 (2017) 323–332.
[25] H.Y. Liu, L.N. Zhang, M. Yan, J.H. Yu, Carbon nanostructures in biology and medicine, J. Mater. Chem. B 5 (2017) 6437–6450.
[26] S. Majdi, A. Jabbari, H. Heli, H. Yadegari, A.A. Moosavi-Movahedi, S. Haghgoo, Electrochemical oxidation and determination of ceftriaxone on a glassy carbon and carbon-nanotube-modified glassy carbon electrodes, J. Solid State Electrochem. 13 (2009) 407–416.
[27] H. Heli, N. Sattarahmady, S.N. Zare, Electrooxidation and determination of perphenazine on a graphene oxide nanosheet modified electrode, RSC Adv. 5 (2015) 21005–21011.
[28] A. Rahi, K. Karimian, H. Heli, Nanostructured materials in electroanalysis of pharmaceuticals, Anal. Biochem. 497 (2016) 39–47.
[29] H. Heli, A. Jabbari, M. Zarghan, A.A. Moosavi-Movahedi, Copper nanoparticles–carbon microparticles nanocomposite for electrooxidation and sensitive detection of sotalol, Sens. Actuators B Chem. 140 (2009) 245–251.
[30] A. Kharin, O. Syshchyk, A. Geloen, S. Alekseev, A. Rogov, V. Lysenko, V. Timoshenko, Carbon fluoroxide nanoparticles fluorescent labels and sonosensitizers for theranostic applications, Sci. Technol. Adv. Mater. 16 (2015) 044601.
[31] N. Yumita, Y. Iwase, T. Imaizumi, A. Sakurazawa, Y. Kaya, K. Nishi, T. Ikeda, S. Umemura, F.S. Chen, Y. Momose, Sonodynamically-induced anticancer effects by functionalized fullerenes, Anticancer Res. 33 (2013) 3145–3151.
[32] E. Peng, F. Wang, J.M. Xue, Nanostructured magnetic nanocomposites as MRI contrast agents, J. Mater. Chem. B 3 (2015) 2241–2276.
[33] S. Shen, L. Wu, J. Liu, M. Xie, H. Shen, X. Qi, Y. Yan, Y. Ge, Y. Jin, Core–shell structured Fe3O4@TiO2-doxorubicin nanoparticles for targeted chemo-sonodynamic therapy of cancer, Int. J. Pharmaceut. 486 (2015) 380–388.
[34] J.D. Trono, K. Mizuno, N. Yusa, T. Matsukawa, K. Yokoyama, M. Uesaka, Size, concentration and incubation time dependence of gold nanoparticle uptake into pancreas cancer cells and its future application to X-ray drug delivery system, J. Radiat. Res. 52 (2011) 103–109.
[35] S. Prijic, J. Scancar, R. Romih, M. Cemazar, V.B. Bregar, A. Znidarsic, G. Sersa, Increased cellular uptake of biocompatible superparamagnetic iron oxide nanoparticles into malignant cells by an external magnetic field, J. Membrane Biol. 236 (2010) 167–179.
[36] M. Gorgizadeh, N. Azarpira, R. Dehdari Veis, N. Sattarahmady, Repression of melanoma tumor in vitro and in vivo by photothermal effect of carbon xerogel nanoparticles, Colloids Surf. B 176 (2019) 449–455.
[37] S. Yamaguchi, H. Kobayashi, T. Narita, K. Kanehira, S. Sonezaki, N. Kudo, Y. Kubota, S. Terasaka, K. Houkin, Sonodynamic therapy using water dispersed TiO2-polyethylene glycol compound on glioma cells: comparison of cytotoxic mechanism with photodynamic therapy, Ultrason. Sonochem. 18 (2011) 1197–1204.
[38] K. Ninomiya, C. Ogino, S. Oshima, S. Sonoke, S. Kuroda, N. Shimizu, Targeted sonodynamic therapy using protein-modified TiO2 nanoparticles, Ultrason. Sonochem. 19 (2012) 607–614.
[39] K. Ninomiya, K. Noda, C. Ogino, S. Kuroda, N. Shimizu, Enhanced OH radical generation by dual-frequency ultrasound with TiO2 nanoparticles: its application to targeted sonodynamic therapy, Ultrason. Sonochem. 21 (2014) 289–294.
[40] S. Xu, Z. Zhou, L. Zhang, Z. Yu, W. Zhang, Y. Wang, X. Wang, M. Li, Y. Chen, C. Chen, M. He, G. Zhang, M. Zhong, Exposure to 1800 MHz radiofrequency radiation induces oxidative damage to mitochondrial DNA in primary cultured neurons, Brain Res. 1311 (2010) 189–196.
[41] J.E. Kennedy, High-intensity focused ultrasound in the treatment of solid tumours, Nat. Rev. Cancer 5 (2005) 321–327.
[42] M. Trendowski, Using the promise of sonodynamic therapy in the clinical setting against disseminated cancers, Chemother. Res. Pract. 2015 (2015) 316015.
[43] S.L. Madanshetty, R.E. Apfel, Acoustic microcavitation: enhancement and applications, J. Acoust. Soc. Am. 90 (1991) 1508–1514.
[44] Y.W. Chen, T.Y. Liu, P.H. Chang, P.H. Hsu, H.L. Liu, H.C. Lina, S.Y. Chen, A theranostic nrGO@MSN-ION nanocarrier developed to enhance the combination effect of sonodynamic therapy and ultrasound hyperthermia for treating tumor, Nanoscale 8 (2016) 12648–12657.
[45] G.T. Clement, Perspectives in clinical uses of high-intensity focused ultrasound, Ultrasonics 42 (2004) 1087–1093.
[46] N. Shimizu, K. Ninomiya, C. Ogino, M.M. Rahman, Potential uses of titanium dioxide in conjunction with ultrasound for improved disinfection, Biochem. Eng. J. 48 (2010) 416–423.
[47] K. Ninomiya, A. Fukuda, C. Ogino, N. Shimizu, Targeted sonocatalytic cancer cell injury using avidin-conjugated titanium dioxide nanoparticles, Ultrason. Sonochem. 21 (2014) 1624–1628.
[48] A.A. Ismail, D.W.J. Bahnemann, Mesostructured Pt/TiO2 nanocomposites as highly active photocatalysts for the photooxidation of dichloroacetic acid, Phys. Chem. C 115 (2011) 5784–5791.
[49] M. Murdoch, G.I. Waterhouse, M.A. Nadeem, J.B. Metson, M.A. Keane, R.F. Howe, J. Llorca, H. Idriss, The effect of gold loading and particle size on photocatalytic hydrogen production from ethanol over Au/TiO2 nanoparticles, Nat. Chem. 3 (2011) 489–492.
[50] V.G. Deepagan, D.G. You, W. Um, H. Ko, S. Kwon, K.Y. Choi, G.R. Yi, J.Y. Lee, D.S. Lee, K. Kim, I.C. Kwon, J.H. Park, Long-circulating Au-TiO2 nanocomposite as a sonosensitizer for ROS-mediated eradication of cancer, Nano Lett. 16 (2016) 6257–6264.
[51] Y. Liu, C.Y. Liu, Q.H. Rong, Z. Zhang, Characteristics of the silver-doped TiO2 nanoparticles, Appl. Surf. Sci. 220 (2003) 7–11.
[52] A.K.W. Wood, C.M. Sehgal, A review of low-intensity ultrasound for cancer therapy, Ultrasound Med. Biol. 41 (2015) 905–928.